AGU ADVANCING EARTH AND SPACE SCIENCES

Geophysical Research Letters

RESEARCH LETTER
10.1029/2024GL108169

Constraining Shear Strength of Fault Damage Zone Using Geodetic Data and Numerical Simulation

Chenglong Li[1], Zhangfeng Ma[2], Xi Xi[1], Guohong Zhang[1], and Xinjian Shan[1]

[1]State Key Laboratory of Earthquake Dynamics, Institute of Geology, China Earthquake Administration, Beijing, China, [2]Earth Observatory of Singapore, Nanyang Technological University, Singapore, Singapore

Key Points:

- Shear modulus and shear stress for coseismic damage zone were determined using coseismic deformation and finite element model
- Estimated shear strength from overlap range of coseismic stress between surface rupture and non-rupture parts ranges from 7 to 17 MPa
- Shear strength exhibits positive and negative correlations with confining pressure and fault maturity, respectively

Supporting Information:

Supporting Information may be found in the online version of this article.

Correspondence to:

X. Shan,
xjshan@ies.ac.cn

Citation:

Li, C., Ma, Z., Xi, X., Zhang, G., & Shan, X. (2024). Constraining shear strength of fault damage zone using geodetic data and numerical simulation. *Geophysical Research Letters*, *51*, e2024GL108169. https://doi.org/10.1029/2024GL108169

Received 14 JAN 2024
Accepted 29 APR 2024

Author Contributions:

Conceptualization: Chenglong Li, Zhangfeng Ma
Formal analysis: Chenglong Li, Guohong Zhang, Xinjian Shan
Funding acquisition: Guohong Zhang, Xinjian Shan
Investigation: Chenglong Li, Zhangfeng Ma, Guohong Zhang
Methodology: Chenglong Li, Zhangfeng Ma, Xi Xi
Project administration: Xinjian Shan
Software: Chenglong Li, Zhangfeng Ma, Xi Xi
Supervision: Xinjian Shan
Validation: Chenglong Li, Guohong Zhang
Writing – original draft: Chenglong Li, Zhangfeng Ma, Xi Xi

Abstract Shear strength of damage zone, representing the stress threshold for rupture initiation, is a critical parameter in faulting mechanics. Despite its significance, the damage-zone's shear strength has not been estimated in natural earthquake ruptures. Here we employed coseismic deformation and strain, kinematic slip model, and finite element modeling to determine the elastic properties and peak shear stress of coseismic damage zones along the 2021 Mw 7.4 Maduo earthquake. Through the analysis of the lowest shear stress resulting in surface ruptures and the highest stress without surface rupture, we constrained the strength within a range of 7–17 MPa. Our result is consistent with strength (5–16 MPa) of sandstone samples from laboratory tests, demonstrating the validity of this estimation. Although factors such as fault maturity and confining pressure influence strength variation, the strength can directly reflect the stress threshold required for macroscopic surface rupture formation in fault damage zones dominated by sandstone.

Plain Language Summary Shear strength of a fault damage zone inform us its ability to withstand shear stress before surface rupture occurs. This information often provides insights into the earthquakes rupture hazards near the Earth's surface. Natural earthquakes provide a perfect opportunity for us to address the question of "what is the shear strength of a fault damage zone." To this end, we require a set of comparative references: the utmost shear stress that a damage zone can withstand without surface rupture and the minimal one necessary for the zone to generate surface rupture. In this investigation, we studied the 2021 Maduo earthquake because it had multiple distinct surface rupture segments in some places but not in others. By comparing shear stress in these segments, we could figure out how strong the damage zones were. We used real observations and numerical simulations to estimate how much stress these damage zones can withstand. Our results indicate that, for damage zones embedded in intact sandstone with a Young's modulus of 15 GPa, its strength ranges from 7 to 17 MPa. Significantly, our study is the first to reveal the shear strength of damage zone from a nutural earthquake using geodetic data.

1. Introduction

For a damage zone embedded in a seismogenic fault, the shear strength is one of its most significant mechanical properties. The shear strength represents the ability that a damage zone can withstand maximum shear stress without generating macroscopic ruptures (Bletery et al., 2016; Faulkner et al., 2010; Fossen, 2016; Fossen & Cavalcante, 2017; Marone et al., 1995; Tenthorey et al., 2003). Compared to the surrounding host rocks, damage zones often exhibit a dense network of fractures, which can be macroscopically approximated as an elastic zone with a reduced elastic modulus (e.g., shear and tensile strength, and stiffness) and seismic velocities (Allam & Ben-Zion, 2012; Biegel & Sammis, 2004; Chester & Logan, 1986; Choi et al., 2016). Damage zones have been found to cause a notable 20%–60% decrease in seismic velocities (Lewis & Ben-Zion, 2010; Lu & Ben-Zion, 2022; Perrin et al., 2016), and to accommodate 28%–88% of distributed, off-fault deformation (Antoine et al., 2021; Dolan & Haravitch, 2014; C. Li et al., 2022; Zinke et al., 2014). Such mechanical response of damage zones during the earthquake cycle may in principle be related to mechanical properties anomalies within the damage zone (Ishii, 2015; Okubo et al., 2019; Shearer, 2019; Thakur et al., 2020). Therefore, understanding shear strength of a damage zone holds significant importance for variable applications, such as assessing rupture mechanics and hazards associated with shallow faults.

The prevalent method to constrain the mechanical properties of rock materials is to conduct laboratory experiments (Hart & Wang, 1995; Ishii, 2015, 2016; Wong & Baud, 2012; Xu, Fukuyama, et al., 2023; Zhou et al., 2018). However, even after a range of tests on host rocks with different lithologies, confining pressures, and

Writing – review & editing: Xinjian Shan

fluid saturations, the shear strength derived from small-scale, intact host rock samples in the laboratory often fails to accurately represent that of larger rock masses (Jónsson, 2012). Other methods for estimating the mechanical properties of damage zones include numerical models (e.g., Bletery et al., 2017; Fang & Dunham, 2013; Huang, 2018; Thakur et al., 2020) and seismic dense arrays (e.g., Zhang et al., 2022; Zhou et al., 2022). Importantly, the shear strength of a damage zone can be significantly influenced by many factors, such as fault maturity (Ikari et al., 2011; Manighetti et al., 2007; Thakur & Huang, 2021), thermal dependence of fault strength (Badt et al., 2020; Di Toro et al., 2011), fault surface topography (Xu, Fukuyama, et al., 2023), and dynamic weakening law (Fang & Dunham, 2013; Xu et al., 2018). Existing methods fail to replicate structures of natural damage zones in a laboratory setting and do not account for dynamic rupture effects during natural earthquakes. Therefore, the assessment of "how much shear stress a fault damage zone can withstand before generating macroscopic rupture" is hindered by the lack of direct estimates from natural earthquake ruptures.

Notably, recent advancements in satellite observations for coseismic deformation and strain have significantly improved our understanding of mechanical properties within fault damage zones, such as fault friction, inelastic failure, rupturing strain limit, and elastic modulus (e.g., Barnhart et al., 2020; C. Li et al., 2023; Milliner et al., 2022; Xu et al., 2020; Xu, Liu, & Lavier, 2023). These efforts enable us to characterize the coseismic strain of the damage zone in great detail, a crucial prerequisite for resolving damage-zone's shear strength in natural earthquake ruptures. Another prerequisite demands the presence of both surface-rupture segments and segments without surface rupture (referred as non-rupture) during a single earthquake. The overlapping range of coseismic shear stress observed along the two types of segments affords us a unique opportunity to directly determine the shear strength of the damage zone. Interestingly, this specific requirement appears to have been met in the 2021 Maduo earthquake (eastern Tibetan Plateau). The Maduo seismogenic fault produced surface rupture segments interspersed with non-rupture segments of a similar spatial scale (Liu-Zeng et al., 2022; Pan et al., 2022; Yuan et al., 2022). In our study, we employed the coseismic deformation and strain, kinematic slip model, and finite element modeling to determine the structural parameters and elastic properties of coseismic damage zones. By combining the maximum shear strain along the Maduo rupture (C. Li et al., 2023), we quantified the peak shear stress imposed by the Maduo rupture, and directly constrained the shear strength of the damage zone.

2. Data and Methods

2.1. Methods of Constraining Shear Strength

Rock deformation commonly undergoes distinct stages defined by two thresholds: yield point and rupture point (Fossen, 2016; Jónsson, 2012; Figure 1). The yield point (i.e., yield strength) marks the transition from elastic to plastic deformation. The rupture point indicates the stress limit the rock can withstand before forming macroscopically fracturing, with the shear stress limit aligning with the shear strength. For the Maduo earthquake, the occurrence of surface rupture depends on whether the peak coseismic shear stress accommodated within the damage zone surpasses its shear strength (Figure 1a). Along the rupture segment R1-6, the coseismic shear stress ($\sigma_{rupture}$) has exceeded both the yield and rupture point of the damage zone because of the presence of surface ruptures (Figure 1b). In contrast, along the non-rupture segment N1-6, the coseismic shear stress ($\sigma_{non\text{-}rupture}$) has not exceeded the rupture threshold of the damage zone because there were no surface ruptures, although it may have exceeded the yield threshold (Figure 1c). We can approximately determine the peak coseismic shear stress using the maximum cosiesmic shear strain ($\varepsilon_{non\text{-}rupture}$ and $\varepsilon_{rupture}$) and elastic shear modulus (G) based on quasi-elastic stress–strain relationship (Figures 1b and 1c).

However, strain hardening results in the occurrence of some inelastic deformation that has a non-linear stress-strain relationship between the yield and rupture points. The previously-mentioned approximation may result in an overestimation of the peak shear stress. However, this overestimation only has limited impact on our stress results. The rationale behind is we further consider the following two key factors. Firstly, near-surface bedrocks primarily undergo brittle deformation mechanism, typically experiencing brittle ruptures once their yielding threshold is exceeded, with little to negligible plastic strain (Cartwright-Taylor et al., 2022; Meyers & Chawla, 2008; Nouri et al., 2022; Wang et al., 2020; Wong & Baud, 2012; Zhou et al., 2018). This implies that the quasi-elastic stress-strain relationship is applicable before rupture occurs. Secondly, the coseismic shear strain is continuous along the entire fault, however they are localized and highly distributed along the rupture and non-rupture segments, respectively (Antoine et al., 2023; C. Li et al., 2023; Figure S1 in Supporting Information S1). As a result, the distributed shear strain of non-rupture segments is insufficient to trigger brittle surface

10.1029/2024GL108169

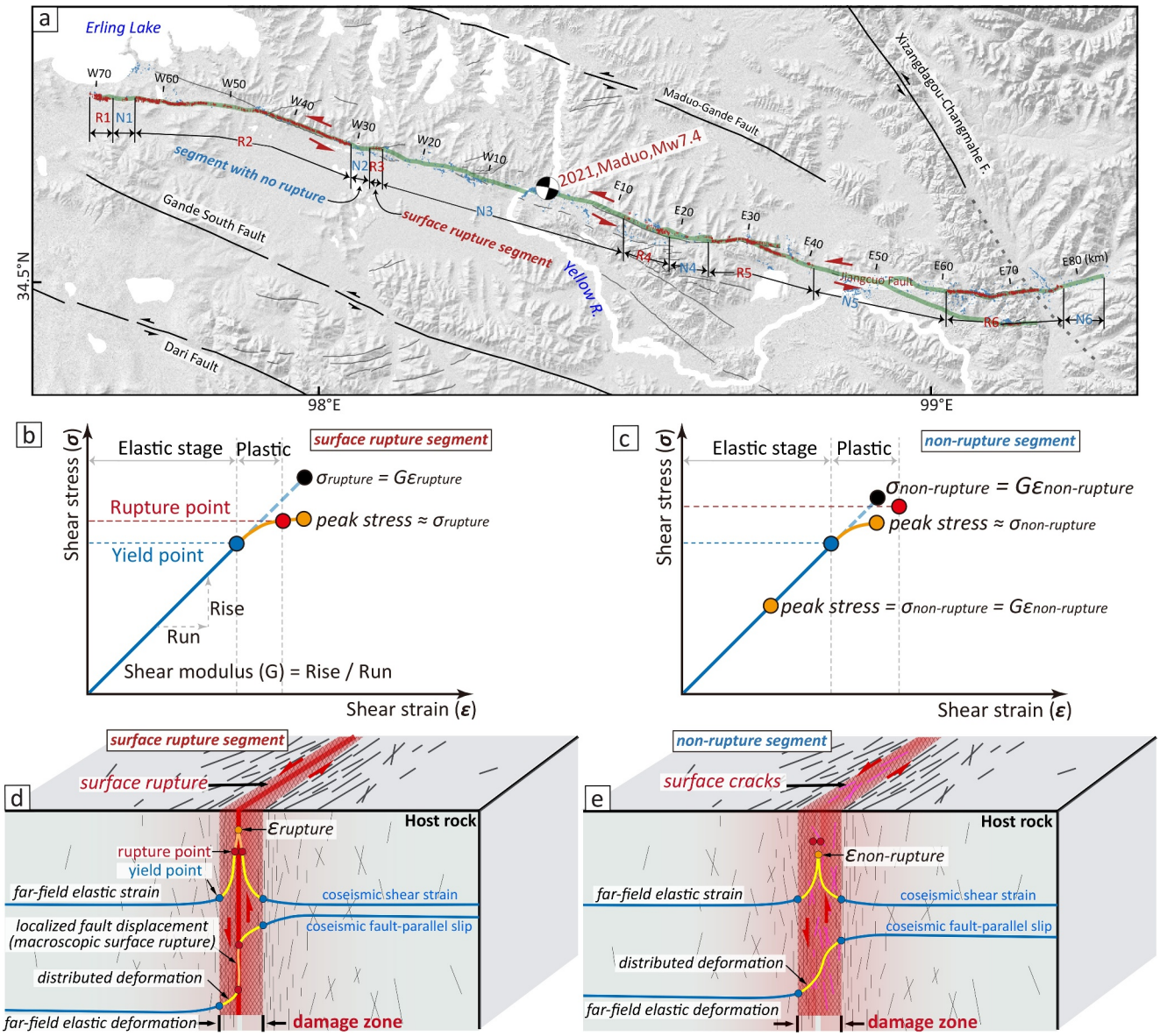

Figure 1. (a) Coseismic surface rupture (R1-6) and non-rupture segments (N1-6) generated by the Maduo earthquake, with geological units. Modified from C. Li et al. (2023). (b, c) Conceptualized shear stress-strain curves of coseismic surface rupture and non-rupture segments, respectively. (d, e) Schematics of coseismic damage zone for surface rupture and non-rupture segments, respectively. Notably, surface rupture can occur when peak coseismic shear stress exceeds strength of a damage zone in panel (d); otherwise, it will not occur in panel (e).

rupture (Liu-Zeng et al., 2022; Pan et al., 2022; Yuan et al., 2022). While some plastic components might be present, coseismic displacements in the non-rupture segments are more likely to be dominated by the quasi-elastic regime. Consequently, the shear stress estimated from the quasi-elastic equation can effectively represent the peak value imposed by the Maduo rupture.

After determining the peak coseismic shear stress, the lowest $\sigma_{rupture}$ in each rupture segment represents the minimum coseismic shear stress required to initiate surface rupture (Figures 1b and 1d). Conversely, the highest $\sigma_{rupture}$ in each non-rupture segment represents the maximum shear stress that damage zone can withstand without developing surface rupture (Figures 1c and 1e). The overlapping range of the lowest $\sigma_{rupture}$ and the highest $\sigma_{non\text{-}rupture}$ represents a critical state of shear stress. In the cases where damage zone experiences coseismic shear stress above this range, surface rupture occurs; whereas surface rupture does not occur. Therefore, the overlapping range of the lowest $\sigma_{rupture}$ and the highest $\sigma_{non\text{-}rupture}$ directly can indicate the shear strength of coseismic damage zone.

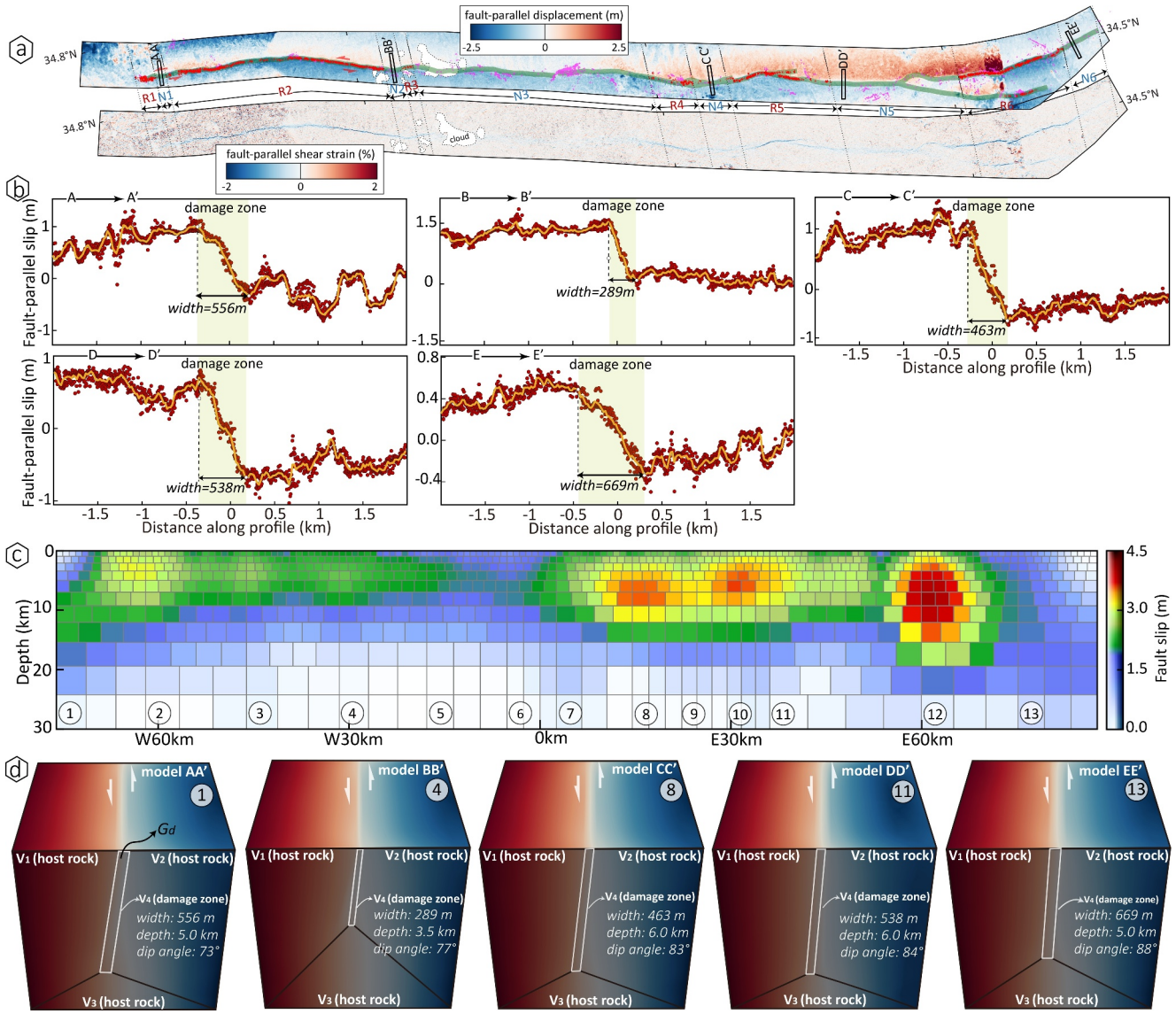

Figure 2. (a) Coseismic fault-parallel displacement and shear strain fields collected from C. Li et al. (2023). (b) Fault-parallel surface displacement along the non-rupture segments N1-6 extracted from the across-fault profiles AA′-EE′ (locations shown in panel a). (c) Coseismic slip distribution of the Maduo fault. (d) FEM setup for analysis of the surface slips across the profile AA′-EE′ buried in a homogeneous medium. The sketch of the model meshes was generated by *Gmsh*, with solution computed by *FEniCS* and visualized in *PyVista* (Sullivan & Kaszynski, 2019).

2.2. Estimating Elastic Properties of the Damage Zone

The estimation of peak shear stress requires quantifying both the maximum shear strain and shear modulus of coseismic damage zones. The maximum shear strain along the Maduo rupture has been measured from the shear strain fields derived from the SPOT satellite optical images (C. Li et al., 2023). Therefore, we only need to determine the shear modulus of coseismic damage zones. To this end, we utilized the geodetic finite element modeling approach from a prior study of Xu, Liu, & Lavier, 2023. Do note that with an assumption of an isotropic linear elastic medium, the system of governing equations is given by linear elasticity. We selected the coseismic displacements in the non-rupture segments N1-6 as our modeling target because these displacements are more likely to be dominated by the elastic regime, therefore more suitable for elastic modeling.

To determine the structural parameters of coseismic damage zones across the segments N1-6, we used five across-fault profiles AA′-EE to extract the fault-parallel displacement from the optical-based displacement field (Figure 2a). The location and width of each coseismic damage zones in the segments N1-6 can be measured from

five displacement profiles (Figure 2b). Additionally, to estimate dip angle and depth of each damage zone, we constructed the fault slip model of the Maduo earthquake using the three-dimensional coseismic deformation resolved from both Sentinel-1 and ALOS-2 images (Liu et al., 2022; Text S1 in Supporting Information S1; Figure 2c and Figures S2–S4 in Supporting Information S1). We determined the structural parameters of each damage zones, including the locations and widths along the profiles AA′-EE′, as well as corresponding depths and optimal dip angles at the fault segment 1, 4, 8, 11, and 13 in our kinematic slip model (Figure 2d).

Based on the structural parameters of five damage zones, we further discretized the meshes using an open-source mesh generator *Gmsh* (Geuzaine & Remacle, 2009). The target damage zones were embedded within a virtual three-dimensional host rock with size of 8 km in the x-, y-, and z-directions, respectively. The shear modulus of the damage zone was then estimated through determining shear modulus reduction ratio (G_d/G_h) between intact host rock with a shear modulus G_h and damage zone (Xu, Liu, & Lavier, 2023). We denote an isotropic linear elastic host rock medium as V_1–V_3. The first scenario is that a shear stress was subjected to an intact rock V_4 embedded within the host rock V_1–V_3 (Figure S5a in Supporting Information S1). The second scenario is that the same shear stress was imposed to a damage zone V_4 embedded within the same host rock V_1–V_3 (Figure S5b in Supporting Information S1). Such differential amount of the shear displacement in the two scenarios should be contributed to reduction in shear modulus between intact host rock and damage zone (Figure S5c in Supporting Information S1). We implemented the FEM to simulate shear displacement in *FEniCS*, an open-source computing platform for solving partial differential equations (Alnæs et al., 2015). The boundary conditions of each model ensured that the strike-slip and dip-slip components matched the estimates from our slip kinematic model (Figure S5 in Supporting Information S1). The bulk and shear modulus for the isotropic materials can be readily well-solved, allowing us to derive the Poisson's ratio (v) from the isotropic stress-strain relationship. To ensure the accuracy of the computational results and reduce computation time, we used an iterative solver based on the Krylov method, with a convergence tolerance of 10^{-14}.

Given that the Maduo earthquake rupture passed through a low-relief mountainous area where Permian-Triassic sandstone is mostly exposed at the surface (Cheng et al., 2006; C. Li et al., 2023; Figure 1), we adopted a Young's modulus of 15 GPa for an intact sandstone based on laboratory experiments, and its shear modulus was further estimated to be 6 GPa based on Poisson's ratio of 0.25 (Fossen, 2016; Nouri et al., 2022). Next, we searched for the optimal G_d/G_h and v, which can result in the best match between the shear displacement simulated by the FEM and the observed surface displacement for the across-fault profiles AA′-EE′ using a MCMC Bayesian sampler (Foreman-Mackey et al., 2013). The goodness of fit between our observed surface displacement and FEM displacement was evaluated using the normalized chi-square misfit. We assumed a uniform prior probability distribution for G_d/G_h and v. Our Monte Carlo Chain produced 1,000 samples of the postprior distribution. The points with highest probability density were used to determine the optimal G_d/G_h and v.

3. Results

The marginal posteriors of shear modulus reduction ratio G_d/G_h and Poisson's ratio v are shown in Figure 3a and Figure S7a in Supporting Information S1. After exploring a range of model parameters, we found that the five preferred shear modulus reduction ratio is 0.10–0.27, and the corresponding Poisson's ratio is 0.25–0.30 (Figure 3b and Figure S7b in Supporting Information S1). This suggests that the strengths of the coseismic damage zone have been decreased to 10%–27% of the intact rock strength. Since the shear modulus of the intact sandstone is assumed to be 15 GPa, we could constrain the shear modulus G_d of the damage zone with a range of 0.6–1.6 GPa (Figure 4a). These shear displacements simulated by the FEM using the preferred model parameters excellently fitted the observed coseismic displacement (Figure 3c and Figure S7c in Supporting Information S1). Subsequently, we collected the maximum shear strain ($\varepsilon_{rupture}$ and $\varepsilon_{non\text{-}rupture}$) along the Maduo rupture (C. Li et al., 2023; Figure 4a). Together with our inferred shear modulus of each damage zone, we further estimated the peak coseismic shear stress along the rupture segments ($\sigma_{rupture} = G_d\varepsilon_{rupture}$) and the non-rupture segments ($\sigma_{non\text{-}rupture} = G_d\varepsilon_{non\text{-}rupture}$) imposed by the Maduo rupture.

However, the mechanical properties of rock materials are closely related to lithology, confining pressures (McBeck et al., 2023; Wang et al., 2020), brittleness (Altındağ & Güney, 2010; Hucka & Das, 1974; Mikaeil et al., 2011; Wang et al., 2014), fluid saturation (Verwer et al., 2010; Yoshida et al., 2016), and pore conditions (e.g., porosity, permeability; Fossen, 2016; Gu et al., 2016; Kaproth et al., 2016; X. Li et al., 2017). To mitigate the potential impact of various factors on the strength estimations, our strengths are inferred from the overlapping

10.1029/2024GL108169

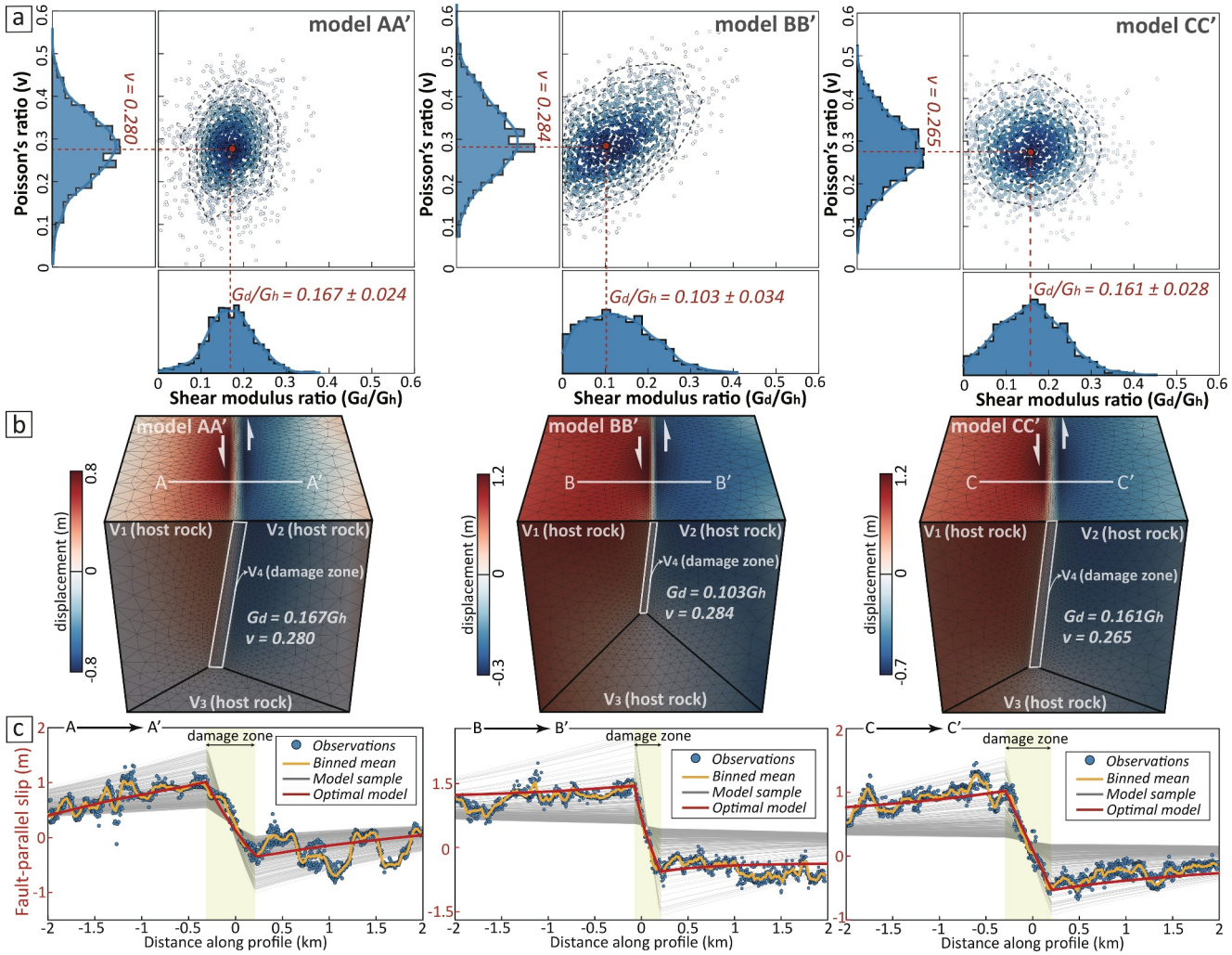

Figure 3. (a) Marginal posteriors of shear modulus ratio (G_d/G_h) and Poisson's ratio (v) for the damage zones along the profile AA′-CC′. The red dots represent the best matching v and G_d/G_h ($\pm 1\sigma$). (b) Displacement distribution in each FEM using the best matching parameters. Remarkably, the inferred shear modulus totally shows an increasing tendency toward the east. (c) Observed and FEM displacement profiles. The black and red lines respectively denote the amplitude of shear displacement for the input model and the best matching samples. Notably, the optimal simulated displacement closely aligns with the observed data.

peak shear stress in the contiguous pairs of surface rupture and non-rupture segments (e.g., R1-N1-R2), which has equivalent space scales (lengths of 2–5 km) and passed through Permian-Triassic sandstone. Other segments were excluded in the strength estimations, including (a) the segments through partially buried beneath unconsolidated Quaternary alluvial, sand-dune and swampy deposits such as at W3-E7 km and E51-E61 km, (b) those parts exceeding 5 km in length (Figures 1a and 4).

For each rupture segment, the lowest $\sigma_{rupture}$ imposed by the Maduo coseismic rupture was determined to be the minimum value among all $\sigma_{rupture}$, with a range of 7–15 MPa (Figure 4b). The lowest $\sigma_{rupture}$ represents the minimum shear stress required to trigger surface rupture within the damage zone. In contrast, all $\sigma_{non\text{-}rupture}$ along non-rupture segments yield six highest values ranging from 8 to 17 MPa (Figure 4b). The highest $\sigma_{non\text{-}rupture}$ signifies the capacity of the damage zone to withstand the utmost shear stress without initiating surface rupture. The overlapping range of the lowest $\sigma_{rupture}$ and highest $\sigma_{non\text{-}rupture}$ in the contiguous pairs directly indicates the shear strength of the damage zone. Therefore, the shear strength of the damage zone varies; it ranges from approximately 14 to 17 MPa near the western (R1-N1-R2), and 12–13 MPa near eastern rupture ends (R6-N6). In the segments R2-N3, the shear strength varies between 7 and 11 MPa. Similarly, from segments N3 to R5, four bounds indicate shear strength values ranging from 8 to 17 MPa. In the segments R5-N5, the shear strength can be constrained to range from 7 to 13 MPa. In general, based on the joint constraints from the five contiguous pairs of

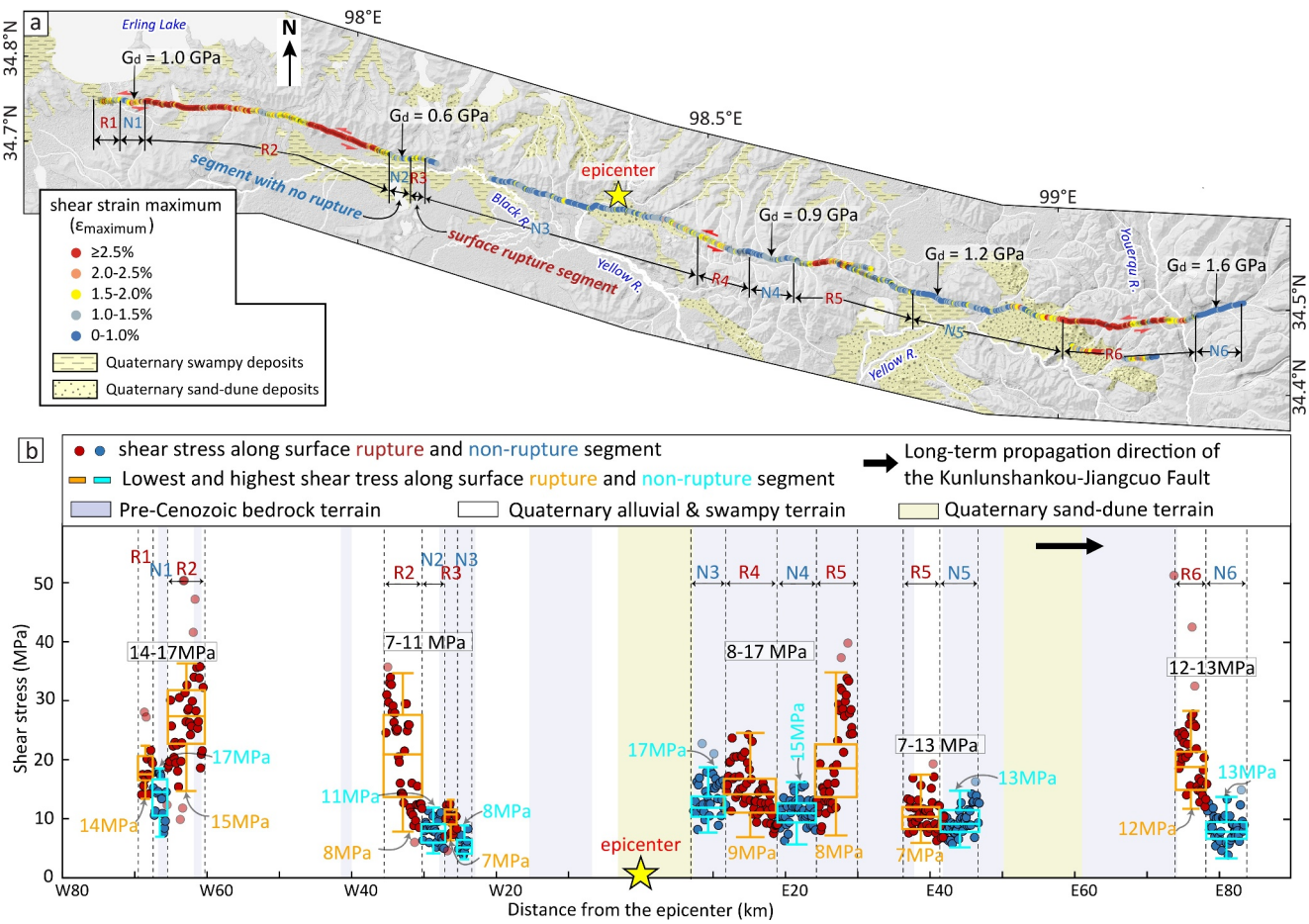

Figure 4. (a) The maximum shear strain along the Maduo earthquake rupture, and the shear modulus of the damage zones. (b) The estimated peak coseismic shear stress imposed by the Maduo rupture. The shear strengths of the damage zones were inferred from the lowest shear stress at the surface rupture segments and the highest at the non-rupture segments.

damage zones, the shear strength required for the formation of coseismic surface rupture should fall within a range of 7–17 MPa. Note that our given shear strength is relative, with the range of 7–17 MPa being derived based on the premise of a Young's modulus of 15 GPa for intact sandstone.

4. Discussions and Conclusions

Our study provides a direct estimate of the shear strength for fault damage zones based on a natural earthquake rupture. Notably, the geophysical significance of our strength represents the maximum shear stress that the damage zone can withstand before generating macroscopic rupture at surface. However, it is essential to note that that our strength estimated in this study only represents static strength at surface or shallowest surface, as surface bedrocks are likely to be significantly lower rigid than rocks at several kilometers deep in the crust (Fossen, 2016; Jónsson, 2012; Rubin & Pollard, 1987). Given the proportionality of shear strength to crust depth, our finding can be further applied to investigate the faulting strength at seismogenic depth (e.g., 5–15 km). Additionally, the Maduo rupture predominantly traversed the Permian-Triassic sandstone, exhibiting no significant along-strike lithological variations (Cheng et al., 2006; C. Li et al., 2023; Figure 1). The damage-zone's shear modulus (G_d) and strength are estimated using the 15 GPa Young's modulus of host sandstone (G_h). Given similar Young's modulus among rocks of the same lithology under normal temperature and pressure, employing a single Young's modulus to estimate shear strength along the Maduo rupture is justifiable. However, we emphasize that our inferred strength values should still be relevant for damage zones that have developed in sandstone-dominated areas. For the damage zone embedded in other rock lithology, it is necessary to use the corresponding Young's modulus to re-estimate shear strength.

We found the shear modulus of the damage zones along the Maduo rupture shows an overall increasing trend from the western to the eastern rupture end (Figure 4a). Previous studies have illustrated that the mechanical properties of fault damage zones systematically depend on fault maturity; young developing faults may exhibit relatively high strength, whereas mature well-slipped faults can be weaker, possibly due to activation of various weakening mechanisms with an increasing cumulative slip (Collettini et al., 2009; Fialko, 2021; Fossen, 2016; Ikari et al., 2011; Manighetti et al., 2007; Thakur & Huang, 2021). It is noted that the Kunlunshankou-Jiangcuo Fault (i.e., the seismogenic fault of the Maduo earthquake) connects with the Eastern Kunlun Fault at its western end and terminates at its eastern end (coincident with the Maduo eastern rupture end), where the slip accumulation is negligible (C. Li et al., 2023; Pan et al., 2022). Consequently, this fault likely has developed through progressive eastward propagation, and therefore, its slip accumulation and structural maturity should decrease toward the east (e.g., Manighetti et al., 2001; Perrin et al., 2016). Given that the rock within the fault damage zone tends to weaken, as fault slip accumulates (e.g., Ben-Zion & Sammis, 2003; Chester & Logan, 1986), the increase in shear modulus toward the east can be explained by the decrease in fault maturity in that direction. The fault zone closer to the eastern end is expected to have lower slip accumulation and maturity, resulting in a less developed gouge zone and, consequently, higher shear strength.

Apart from the fault maturity, the along-strike variation of the shear strength may be due to several potential factors, including rock lithology, coseismic dynamic weakening, and loading conditions like confining pressure, temperature, and the presence of fluids (Figure 4b; Badt et al., 2020; Di Toro et al., 2011; Fang & Dunham, 2013; Jamtveit et al., 2019; Wang et al., 2020; Xu, Fukuyama, et al., 2023; Xu et al., 2018). Along the Maduo earthquake fault, the predominant bedrock consists of Permian-Triassic sandstone (Figure 1). Despite the presence of Quaternary deposits covering on the bedrock, our strength values should still be relevant for damage zones that have developed in sandstone-dominated areas. For example, the strength (8–15 MPa) from the bedrock terrain between the segments N4-R5 is seemly lower than that (12–13 MPa) from the Quaternary alluvial terrain at the segments R6-N6. This contradicts the expectation that the terrain with softer Quaternary deposits has a lower strength (Figure 4; Cheng et al., 2006). This variation of shear strength cannot be attributed solely to the difference in rock lithology.

The confining pressure has a significant sensitivity to the rock mechanical properties. With the increase of confining pressure, the rock deformation undergoes transformation process from brittle failure to ductile deformation, and the shear strength also increases (Wang et al., 2020). At a rough estimate, the Quaternary deposits with a thickness of <200 m would impose crustal confining pressure of <5 MPa (lithostatic stress $\sigma = \rho g h = 2{,}584\ \mathrm{kg/m^3} \times 9.8\ \mathrm{m/s^2} \times 200\ m$) to the coseismic damage zone (Cheng et al., 2006; Fialko, 2021; Huang et al., 2020; Figure 1a). For example, (a) the parts R2-N2 covered by the Quaternary deposits was inferred a strength range of 8–11 MPa, and nearby bedrock-terrain segments R3-N3 has a relative lower strength of 7–8 MPa; (b) the strength of the rupture segments (i.e., R1, R2, and R6); covered by the Quaternary deposits is significantly larger than that at the bedrock-terrain rupture segments (Figure 4b). This suggests that the confining pressure imposed by the Quaternary deposits positively influences the shear strength. The relatively low confining pressure of 5 MPa does typically not change the rock brittleness such that our above assumption is still applicable (Wang et al., 2020); however, as confining pressure increases, the shear strength of the damage zone is also likely to rise.

Except for the factors mentioned, temperature can also have an impact on fault strength (Fossen, 2016). In our investigation, the near-surface areas typically remain at ordinary temperature conditions, and the temperature changes are not significant enough to cause substantial variations in fault shear strength. However, it is necessary to take into account coseismic dynamic weakening that can occur due to high slip rates (Chang et al., 2012; Xu et al., 2018). For example, at high seismic slip rates, there is a remarkable decrease in the friction coefficient of crustal silicate rocks due to intense "flash" heating of microscopic asperity contacts, leading to a degradation of their shear strengths (Goldsby & Tullis, 2011). During the Maduo rupture, the estimated coseismic slip rate was approximately (at most) 0.4 m/s near the E30 km, decreasing to less than 0.1 m/s at both the western and eastern rupture ends. Paradoxically, the strengths at these ends are higher, which is in clear contradiction to the expected degradation of fault shear strength caused by a fast slip rate. The variation in strength does not appear to be attributable to the seismic slip rate either, as the inverted coseismic slip rates are remarkably consistent (0.2–0.3 m/s) across all measurement sites (Fang et al., 2022). Furthermore, our derived shear strengths are comparable to laboratory measurements on the intact siliceous mudstones and Cenozoic-Mesozoic sandstones. When considering shear modulus reduction of damage zone compared to intact rocks, the shear strength of 7–17 MPa is

consistent with those of intact siliceous mudstone samples (6–19 MPa) and sandstone samples (5–16 MPa) tested on various conditions (Ishii, 2015; Nouri et al., 2022; Figure S8 in Supporting Information S1). Most importantly, compared to laboratory measurements, our estimations provide a more comprehensive reflection of natural damage zones' ability to withstand coseismic shear stress, as they incorporate interactions of various weakening mechanisms and tectonic conditions during natural earthquake ruptures.

In conclusion, we employed coseismic deformation and strain, kinematic slip model, and finite element modeling to determine the elastic properties and peak shear stress of coseismic damage zones. Our results revealed that for the damage zone embedded in an intact sandstone with a Young's modulus of 15 GPa, its shear strength can be estimated to range from 7 to 17 MPa. Our findings also suggest that shear strength of damage zone is positively correlated with confining pressure and negatively with fault maturity, respectively. Overall, our estimations reflect the capacity of natural damage zones in sandstone-dominated areas to withstand coseismic shear stress without initiating macroscopic rupture.

Data Availability Statement

Coseismic surface rupture and shear-strain data related to the Maduo earthquake are accessible from (C. Li et al., 2023; Yuan et al., 2022), respectively. Auxiliary materials of the manuscript, including the shear stress and strength along the Maduo rupture we estimated and the codes of finite element model, have been uploaded at (C. Li et al., 2024).

Acknowledgments
This study is co-supported by the National Natural Science Foundation of China (Grant U2139202), the National Nonprofit Fundamental Research of Institute of Geology, China Earthquake Administration (Grant IGCEA2005), and by the China Scholarship Council scholarship (Grant 202204190006). We thank Haipeng Luo, River Shaoneng He for fruitful discussions.

References

Allam, A. A., & Ben-Zion, Y. (2012). Seismic velocity structures in the southern California plate-boundary environment from double-difference tomography. *Geophysical Journal International*, *190*(2), 1181–1196. https://doi.org/10.1111/j.1365-246x.2012.05544.x

Alnæs, M., Blechta, J., Hake, J., Johansson, A., Kehlet, B., Logg, A., et al. (2015). The FEniCS project version 1.5. *Archive of Numerical Software*, *3*(100). https://doi.org/10.11588/ans.2015.100.20553

Altındağ, R., & Güney, A. (2010). Predicting the relationships between brittleness and mechanical properties (UCS, TS and SH) of rocks. Retrieved from https://hdl.handle.net/20.500.12809/4536

Antoine, S. L., Klinger, Y., Delorme, A., Wang, K., Bürgmann, R., & Gold, R. D. (2021). Diffuse deformation and surface faulting distribution from submetric image correlation along the 2019 Ridgecrest, California, ruptures. *Bulletin of the Seismological Society of America*, *111*(5), 2275–2302. https://doi.org/10.1785/0120210036

Antoine, S. L., Liu, Z., Klinger, Y., Delorme, A., & Liu-Zeng, J. (2023). Characterizing the transition from diffuse to localized deformation using optical image correlation: The 2021 Mw7. 4 Maduo, Tibet, earthquake (No. EGU23-16845). Copernicus Meetings.

Badt, N. Z., Tullis, T. E., Hirth, G., & Goldsby, D. L. (2020). Thermal pressurization weakening in laboratory experiments. *Journal of Geophysical Research: Solid Earth*, *125*(5), e2019JB018872. https://doi.org/10.1029/2019jb018872

Barnhart, W. D., Gold, R. D., & Hollingsworth, J. (2020). Localized fault-zone dilatancy and surface inelasticity of the 2019 Ridgecrest earthquakes. *Nature Geoscience*, *13*(10), 699–704. https://doi.org/10.1038/s41561-020-0628-8

Ben-Zion, Y., & Sammis, C. G. (2003). Characterization of fault zones. *Pure and Applied Geophysics*, *160*(3), 677–715. https://doi.org/10.1007/pl00012554

Biegel, R. L., & Sammis, C. G. (2004). Relating fault mechanics to fault zone structure. *Advances in Geophysics*, *47*, 65–111. https://doi.org/10.1016/s0065-2687(04)47002-2

Bletery, Q., Thomas, A. M., Rempel, A. W., & Hardebeck, J. L. (2017). Imaging shear strength along subduction faults. *Geophysical Research Letters*, *44*(22), 11329–11339. https://doi.org/10.1002/2017GL075501

Bletery, Q., Thomas, A. M., Rempel, A. W., Karlstrom, L., Sladen, A., & De Barros, L. (2016). Mega-earthquakes rupture flat megathrusts. *Science*, *354*(6315), 1027–1031. https://doi.org/10.1126/science.aag0482

Cartwright-Taylor, A., Mangriotis, M. D., Main, I. G., Butler, I. B., Fusseis, F., Ling, M., et al. (2022). Seismic events miss important kinematically governed grain scale mechanisms during shear failure of porous rock. *Nature Communications*, *13*(1), 6169. https://doi.org/10.1038/s41467-022-33855-z

Chang, J. C., Lockner, D. A., & Reches, Z. (2012). Rapid acceleration leads to rapid weakening in earthquake-like laboratory experiments. *Science*, *338*(6103), 101–105. https://doi.org/10.1126/science.1221195

Cheng, J., Zhang, X., Tian, M., Zan, L., Tang, D., Yue, J., & Yu, W. (2006). *Quaternary geology and ecological environment in the source area of the Yellow River* (p. 182). Geological Publishing House.

Chester, F. M., & Logan, J. M. (1986). Implications for mechanical properties of brittle faults from observations of the Punchbowl fault zone, California. *Pure and Applied Geophysics*, *124*(1), 79–106. https://doi.org/10.1007/bf00875720

Choi, J. H., Edwards, P., Ko, K., & Kim, Y. S. (2016). Definition and classification of fault damage zones: A review and a new methodological approach. *Earth-Science Reviews*, *152*, 70–87. https://doi.org/10.1016/j.earscirev.2015.11.006

Collettini, C., Niemeijer, A., Viti, C., & Marone, C. (2009). Fault zone fabric and fault weakness. *Nature*, *462*(7275), 907–910. https://doi.org/10.1038/nature08585

Di Toro, G., Han, R., Hirose, T., De Paola, N., Nielsen, S., Mizoguchi, K., et al. (2011). Fault lubrication during earthquakes. *Nature*, *471*(7339), 494–498. https://doi.org/10.1038/nature09838

Dolan, J., & Haravitch, B. (2014). How well do surface slip measurements track slip at depth in large strike-slip earthquakes? The importance of fault structural maturity in controlling on-fault slip versus off-fault surface deformation. *Earth and Planetary Science Letters*, *388*, 38–47. https://doi.org/10.1016/j.epsl.2013.11.043

Fang, J., Ou, Q., Wright, T. J., Okuwaki, R., Amey, R. M., Craig, T. J., et al. (2022). Earthquake cycle deformation associated with the 2021 MW 7.4 Maduo (Eastern Tibet) earthquake: An intrablock rupture event on a slow-slipping fault from Sentinel-1 InSAR and teleseismic data. *Journal of Geophysical Research: Solid Earth*, *127*(11), e2022JB024268. https://doi.org/10.1029/2022jb024268

Fang, Z., & Dunham, E. M. (2013). Additional shear resistance from fault roughness and stress levels on geometrically complex faults. *Journal of Geophysical Research: Solid Earth*, *118*(7), 3642–3654. https://doi.org/10.1002/jgrb.50262

Faulkner, D. R., Jackson, C. A. L., Lunn, R. J., Schlische, R. W., Shipton, Z. K., Wibberley, C. A. J., & Withjack, M. O. (2010). A review of recent developments concerning the structure, mechanics and fluid flow properties of fault zones. *Journal of Structural Geology*, *32*(11), 1557–1575. https://doi.org/10.1016/j.jsg.2010.06.009

Fialko, Y. (2021). Estimation of absolute stress in the hypocentral region of the 2019 Ridgecrest, California, earthquakes. *Journal of Geophysical Research: Solid Earth*, *126*(7), e2021JB022000. https://doi.org/10.1029/2021jb022000

Foreman-Mackey, D., Hogg, D. W., Lang, D., & Goodman, J. (2013). emcee: The MCMC hammer. *Publications of the Astronomical Society of the Pacific*, *125*(925), 306–312. https://doi.org/10.1086/670067

Fossen, H. (2016). *Structural geology*. Cambridge University Press.

Fossen, H., & Cavalcante, G. C. G. (2017). Shear zones–A review. *Earth-Science Reviews*, *171*, 434–455. https://doi.org/10.1016/j.earscirev.2017.05.002

Geuzaine, C., & Remacle, J. F. (2009). Gmsh: A 3-D finite element mesh generator with built-in pre-and post-processing facilities. *International Journal for Numerical Methods in Engineering*, *79*(11), 1309–1331. https://doi.org/10.1002/nme.2579

Goldsby, D. L., & Tullis, T. E. (2011). Flash heating leads to low frictional strength of crustal rocks at earthquake slip rates. *Science*, *334*(6053), 216–218. https://doi.org/10.1126/science.1207902

Gu, C., Wang, J., Cai, Y., Sun, L., Wang, P., & Dong, Q. (2016). Deformation characteristics of overconsolidated clay sheared under constant and variable confining pressure. *Soils and Foundations*, *56*(3), 427–439. https://doi.org/10.1016/j.sandf.2016.04.009

Hart, D. J., & Wang, H. F. (1995). Laboratory measurements of a complete set of poroelastic moduli for Berea sandstone and Indiana limestone. *Journal of Geophysical Research: Solid Earth*, *100*(B9), 17741–17751. https://doi.org/10.1029/95jb01242

Huang, S., Yao, H., Lu, Z., Tian, X., Zheng, Y., Wang, R., et al. (2020). High-resolution 3-D shear wave velocity model of the Tibetan Plateau: Implications for crustal deformation and porphyry Cu deposit formation. *Journal of Geophysical Research: Solid Earth*, *125*(7), e2019JB019215. https://doi.org/10.1029/2019jb019215

Huang, Y. (2018). Earthquake rupture in fault zones with along-strike material heterogeneity. *Journal of Geophysical Research: Solid Earth*, *123*(11), 9884–9898. https://doi.org/10.1029/2018JB016354

Hucka, V., & Das, B. (1974). Brittleness determination of rocks by different methods. *International Journal of Rock Mechanics and Mining Sciences and Geomechanics Abstracts*, *11*(10), 389–392. https://doi.org/10.1016/0148-9062(74)91109-7

Ikari, M. J., Marone, C., & Saffer, D. M. (2011). On the relation between fault strength and frictional stability. *Geology*, *39*(1), 83–86. https://doi.org/10.1130/g31416.1

Ishii, E. (2015). Predictions of the highest potential transmissivity of fractures in fault zones from rock rheology: Preliminary results. *Journal of Geophysical Research: Solid Earth*, *120*(4), 2220–2241. https://doi.org/10.1002/2014JB011756

Ishii, E. (2016). Far-field stress dependency of the failure mode of damage-zone fractures in fault zones: Results from laboratory tests and field observations of siliceous mudstone. *Journal of Geophysical Research: Solid Earth*, *121*(1), 70–91. https://doi.org/10.1002/2015JB012238

Jamtveit, B., Petley-Ragan, A., Incel, S., Dunkel, K. G., Aupart, C., Austrheim, H., et al. (2019). The effects of earthquakes and fluids on the metamorphism of the lower continental crust. *Journal of Geophysical Research: Solid Earth*, *124*(8), 7725–7755. https://doi.org/10.1029/2018jb016461

Jónsson, S. (2012). Tensile rock mass strength estimated using InSAR. *Geophysical Research Letters*, *39*(21). https://doi.org/10.1029/2012gl053309

Kaproth, B. M., Kacewicz, M., Muhuri, S., & Marone, C. (2016). Permeability and frictional properties of halite-clay-quartz faults in marine-sediment: The role of compaction and shear. *Marine and Petroleum Geology*, *78*, 222–235. https://doi.org/10.1016/j.marpetgeo.2016.09.011

Lewis, M. A., & Ben-Zion, Y. (2010). Diversity of fault zone damage and trapping structures in the Parkfield section of the San Andreas Fault from comprehensive analysis of near fault seismograms. *Geophysical Journal International*, *183*(3), 1579–1595. https://doi.org/10.1111/j.1365-246x.2010.04816.x

Li, C., Li, T., Hollingsworth, J., Zhang, Y., Qian, L., & Shan, X. (2023). Strain threshold for the formation of coseismic surface rupture. *Geophysical Research Letters*, *50*(16), e2023GL103666. https://doi.org/10.1029/2023GL103666

Li, C., Li, T., Shan, X., & Zhang, G. (2022). Extremely large off-fault deformation during the 2021 M_w 7.4 Maduo, Tibetan plateau, earthquake. *Seismological Research Letters*, *94*(1), 39–51. https://doi.org/10.1785/0220220139

Li, C., Ma, Z., Xi, X., Zhang, G., & Shan, X. (2024). Constraining shear strength of fault damage zone using geodetic data and numerical simulation [Software]. *Zenodo*. https://doi.org/10.5281/zenodo.11096573

Li, X., Gong, F., Tao, M., Dong, L., Du, K., Ma, C., et al. (2017). Failure mechanism and coupled static-dynamic loading theory in deep hard rock mining: A review. *Journal of Rock Mechanics and Geotechnical Engineering*, *9*(4), 767–782. https://doi.org/10.1016/j.jrmge.2017.04.004

Liu, J., Hu, J., Li, Z., Ma, Z., Wu, L., Jiang, W., et al. (2022). Complete three-dimensional coseismic displacements due to the 2021 Maduo earthquake in Qinghai Province, China from Sentinel-1 and ALOS-2 SAR images. *Science China Earth Sciences*, *65*(4), 687–697.

Liu-Zeng, J., Yao, W., Liu, X., Shao, Y., Wang, W., Han, L., et al. (2022). High-resolution structure-from-motion models covering 160 km-long surface ruptures of the 2021 MW 7.4 Madoi earthquake in northern Qinghai-Tibetan Plateau. *Earthquake Research Advances*, *2*(2), 100140. https://doi.org/10.1016/j.eqrea.2022.100140

Lu, Y., & Ben-Zion, Y. (2022). Regional seismic velocity changes following the 2019 M w 7.1 Ridgecrest, California earthquake from auto-correlations and P/S converted waves. *Geophysical Journal International*, *228*(1), 620–630. https://doi.org/10.1093/gji/ggab350

Manighetti, I., Campillo, M., Bouley, S., & Cotton, F. (2007). Earthquake scaling, fault segmentation, and structural maturity. *Earth and Planetary Science Letters*, *253*(3–4), 429–438. https://doi.org/10.1016/j.epsl.2006.11.004

Manighetti, I., King, G. C. P., Gaudemer, Y., Scholz, C. H., & Doubre, C. (2001). Slip accumulation and lateral propagation of active normal faults in Afar. *Journal of Geophysical Research: Solid Earth*, *106*(B7), 13667–13696. https://doi.org/10.1029/2000jb900471

Marone, C., Vidale, J. E., & Ellsworth, W. L. (1995). Fault healing inferred from time dependent variations in source properties of repeating earthquakes. *Geophysical Research Letters*, *22*(22), 3095–3098. https://doi.org/10.1029/95gl03076

McBeck, J., Cordonnier, B., Ben-Zion, Y., & Renard, F. (2023). The influence of confining pressure and preexisting damage on strain localization in fluid-saturated crystalline rocks in the upper crust. *Journal of Geophysical Research: Solid Earth*, *128*(8), e2023JB026987. https://doi.org/10.1029/2023jb026987

Meyers, M. A., & Chawla, K. K. (2008). *Mechanical behavior of materials*. Cambridge University Press.

Mikaeil, R., Ozcelik, Y., Ataei, M., & Yousefi, R. (2011). Correlation of specific ampere draw with rock brittleness indexes in rock sawing process. *Archives of Mining Sciences*, *56*(4), 777–788.
Milliner, C. W. D., Aati, S., & Avouac, J. P. (2022). Fault friction derived from fault bend influence on coseismic slip during the 2019 Ridgecrest Mw 7.1 mainshock. *Journal of Geophysical Research: Solid Earth*, *127*(11), e2022JB024519. https://doi.org/10.1029/2022jb024519
Nouri, M., Khanlari, G., Rafiei, B., Sarfarazi, V., & Zaheri, M. (2022). Estimation of brittleness indexes from petrographic characteristics of different sandstone types (cenozoic and mesozoic sandstones), Markazi Province, Iran. *Rock Mechanics and Rock Engineering*, *55*(4), 1955–1995. https://doi.org/10.1007/s00603-021-02441-y
Okubo, K., Bhat, H. S., Rougier, E., Marty, S., Schubnel, A., Lei, Z., et al. (2019). Dynamics, radiation, and overall energy budget of earthquake rupture with coseismic off-fault damage. *Journal of Geophysical Research: Solid Earth*, *124*(11), 11771–11801. https://doi.org/10.1029/2019jb017304
Pan, J., Li, H., Chevalier, M. L., Tapponnier, P., Bai, M., Li, C., et al. (2022). Co-seismic rupture of the 2021, Mw7. 4 Maduo earthquake (Northern Tibet): Short-cutting of the kunlun fault big bend. *Earth and Planetary Science Letters*, *594*, 117703. https://doi.org/10.1016/j.epsl.2022.117703
Perrin, C., Manighetti, I., Ampuero, J.-P., Cappa, F., & Gaudemer, Y. (2016). Location of largest earthquake slip and fast rupture controlled by along-strike change in fault structural maturity due to fault growth. *Journal of Geophysical Research: Solid Earth*, *121*(5), 3666–3685. https://doi.org/10.1002/2015JB012671
Rubin, A. M., & Pollard, D. P. (1987). Origins of blade-like dikes in volcanic rift zones. In R. W. Decker, T. L. Wright, & P. H. Stauffer (Eds.), *Volcanism in Hawaii* (Vol. 1350, pp. 1449–1470). US Geological Survey Professional Paper.
Shearer, P. M. (2019). *Introduction to seismology* (p. 32). Cambridge University Press.
Sullivan, C., & Kaszynski, A. (2019). PyVista: 3D plotting and mesh analysis through a streamlined interface for the Visualization Toolkit (VTK). *Journal of Open Source Software*, *4*(37), 1450. https://doi.org/10.21105/joss.01450
Tenthorey, E., Cox, S. F., & Todd, H. F. (2003). Evolution of strength recovery and permeability during fluid–rock reaction in experimental fault zones. *Earth and Planetary Science Letters*, *206*(1–2), 161–172. https://doi.org/10.1016/s0012-821x(02)01082-8
Thakur, P., & Huang, Y. (2021). Influence of fault zone maturity on fully dynamic earthquake cycles. *Geophysical Research Letters*, *48*(17), e2021GL094679. https://doi.org/10.1029/2021gl094679
Thakur, P., Huang, Y., & Kaneko, Y. (2020). Effects of low-velocity fault damage zones on long-term earthquake behaviors on mature strike-slip faults. *Journal of Geophysical Research: Solid Earth*, *125*(8), e2020JB019587. https://doi.org/10.1029/2020JB019587
Verwer, K., Eberli, G., Baechle, G., & Weger, R. (2010). Effect of carbonate pore structure on dynamic shear moduli. *Geophysics*, *75*(1), E1–E8. https://doi.org/10.1190/1.3280225
Wang, S., Zhao, W., Fu, X., Zhang, Z., Wang, T., & Ge, J. (2020). A universal method for quantitatively evaluating rock brittle-ductile transition behaviors. *Journal of Petroleum Science and Engineering*, *195*, 107774. https://doi.org/10.1016/j.petrol.2020.107774
Wang, S. Y., Sloan, S. W., Sheng, D. C., Yang, S. Q., & Tang, C. A. (2014). Numerical study of failure behaviour of pre-cracked rock specimens under conventional triaxial compression. *International Journal of Solids and Structures*, *51*(5), 1132–1148. https://doi.org/10.1016/j.ijsolstr.2013.12.012
Wong, T. F., & Baud, P. (2012). The brittle-ductile transition in porous rock: A review. *Journal of Structural Geology*, *44*, 25–53. https://doi.org/10.1016/j.jsg.2012.07.010
Xu, S., Fukuyama, E., Yamashita, F., Kawakata, H., Mizoguchi, K., & Takizawa, S. (2023). Fault strength and rupture process controlled by fault surface topography. *Nature Geoscience*, *16*(1), 94–100. https://doi.org/10.1038/s41561-022-01093-z
Xu, S., Fukuyama, E., Yamashita, F., Mizoguchi, K., Takizawa, S., & Kawakata, H. (2018). Strain rate effect on fault slip and rupture evolution: Insight from meter-scale rock friction experiments. *Tectonophysics*, *733*, 209–231. https://doi.org/10.1016/j.tecto.2017.11.039
Xu, X., Liu, D., & Lavier, L. (2023). Constraining fault damage zone properties from geodesy: A case study near the 2019 Ridgecrest earthquake sequence. *Geophysical Research Letters*, *50*(5), e2022GL101692. https://doi.org/10.1029/2022gl101692
Xu, X., Sandwell, D. T., Ward, L. A., Milliner, C. W., Smith-Konter, B. R., Fang, P., & Bock, Y. (2020). Surface deformation associated with fractures near the 2019 Ridgecrest earthquake sequence. *Science*, *370*(6516), 605–608. https://doi.org/10.1126/science.abd1690
Yoshida, K., Hasegawa, A., & Yoshida, T. (2016). Temporal variation of frictional strength in an earthquake swarm in NE Japan caused by fluid migration. *Journal of Geophysical Research: Solid Earth*, *121*(8), 5953–5965. https://doi.org/10.1002/2016jb013022
Yuan, Z., Li, T., Su, P., Sun, H., Ha, G., Guo, P., et al. (2022). Large surface-rupture gaps and low surface fault slip of the 2021 Mw 7.4 Maduo earthquake along a low-activity strike-slip fault, Tibetan Plateau. *Geophysical Research Letters*, *49*(6), e2021GL096874. https://doi.org/10.1029/2021gl096874
Zhang, Z., Deng, Y., Qiu, H., Peng, Z., & Liu-Zeng, J. (2022). High-Resolution imaging of Fault zone structure along the creeping section of the Haiyuan fault, NE Tibet, from data recorded by dense seismic arrays. *Journal of Geophysical Research: Solid Earth*, *127*(9), e2022JB024468. https://doi.org/10.1029/2022jb024468
Zhou, X. P., Lian, Y. J., Wong, L. N. Y., & Berto, F. (2018). Understanding the fracture behavior of brittle and ductile multi-flawed rocks by uniaxial loading by digital image correlation. *Engineering Fracture Mechanics*, *199*, 438–460. https://doi.org/10.1016/j.engfracmech.2018.06.007
Zhou, Z., Bianco, M., Gerstoft, P., & Olsen, K. (2022). High-resolution imaging of complex shallow fault zones along the July 2019 Ridgecrest ruptures. *Geophysical Research Letters*, *49*(1), e2021GL095024. https://doi.org/10.1029/2021gl095024
Zinke, R., Hollingsworth, J., & Dolan, J. F. (2014). Surface slip and off-fault deformation patterns in the 2013 Mw 7.7 Balochistan, Pakistan earthquake: Implications for controls on the distribution of near-surface coseismic slip. *Geochemistry, Geophysics, Geosystems*, *15*(12), 5034–5050. https://doi.org/10.1002/2014gc005538

References From the Supporting Information

Okada, Y. (1985). Surface deformation due to shear and tensile faults in a half-space. *Bulletin of the Seismological Society of America*, *75*(4), 1135–1154.
Lohman, R. B., & Barnhart, W. D. (2010). Evaluation of earthquake triggering during the 2005– 2008 earthquake sequence on Qeshm Island, Iran. *Journal of Geophysical Research: Solid Earth*, *115*(B12). https://doi.org/10.1029/2010JB007710
Jin, Z., & Fialko, Y. (2020). Finite slip models of the 2019 Ridgecrest earthquake sequence constrained by space geodetic data and aftershock locations. *Bulletin of the Seismological Society of America*, *110*(4), 1660–1679.
Xu, X., Tong, X., Sandwell, D. T., Milliner, C. W., Dolan, J. F., Hollingsworth, J., et al. (2016). Refining the shallow slip deficit. *Geophysical Journal International*, *204*(3), 1867–1886.